J. Fluid Mech. (2010), *vol.* 662, *pp.* 173–196. © Cambridge University Press 2010
doi:10.1017/S0022112010003150

Temporal instability modes of supersonic round jets

LUIS PARRAS[1,2]† AND STÉPHANE LE DIZÈS[1]

[1]IRPHE-CNRS & Aix-Marseille University, 49 rue F. Joliot-Curie, F-13013 Marseille, France
[2]Universidad de Málaga, E. T. S. Ingenieros Industriales, 29071 Málaga, Spain

(Received 18 December 2009; revised 8 June 2010; accepted 8 June 2010;
first published online 1 September 2010)

In this study, a comprehensive inviscid temporal stability analysis of a compressible round jet is performed for Mach numbers ranging from 1 to 10. We show that in addition to the Kelvin–Helmholtz instability modes, there exist for each azimuthal wavenumber three other types of modes (counterflow subsonic waves, subsonic waves and supersonic waves) whose characteristics are analysed in detail using a WKBJ theory in the limit of large axial wavenumber. The theory is constructed for any velocity and temperature profile. It provides the phase velocity and the spatial structure of the modes and describes qualitatively the effects of base-flow modifications on the mode characteristics. The theoretical predictions are compared with numerical results obtained for an hyperbolic tangent model and a good agreement is demonstrated. The results are also discussed in the context of jet noise. We show how the theory can be used to determine *a priori* the impact of jet modifications on the noise induced by instability.

Key words: jet noise, instability

1. Introduction

Stability of supersonic jet flows has been a widely studied subject over the past half century owing to its importance in the development of supersonic aircraft. Nowadays, the main interest of this research topic has moved to understanding how jet instabilities are related to sound waves, and how to act on the flow to reduce the sound-wave emission. Since the seminal work of Lighthill (1952) on sound theory, it has been known that sound is mainly produced by instabilities and turbulence. A review of the different sources of noise in supersonic jets has been done by Tam (1995). He argued that supersonic jet noise consists of three main components: turbulent mixing noise containing both large-scale and fine-scale contributions, broadband shock noise and screech tones. The turbulence mixing noise is mainly associated with the shear-layer instability of the jet as demonstrated by Tam & Burton (1984*a*) for two-dimensional jets and by Tam & Burton (1984*b*) for round jets. The two other sources of noise are due to shocks and are present when the jet is not perfectly expanded. They can be theoretically eliminated by acting on the jet pressure. By contrast, mixing noise is much more difficult to control.

The shear-layer instability (also called Kelvin–Helmholtz instability) has been initially studied in two-dimensional incompressible flows. Michalke (1964) performed

---

† Email address for correspondence: lparras@uma.es

the first stability analysis of a shear layer with an hyperbolic tangent profile. Later, Blumen (1970) extended Michalke's results to compressible flows, obtaining a neutral instability curve for Mach numbers $M \leqslant 1$. At first, his results were in disagreement with earlier results by Drazin & Howard (1966) and with the theoretical condition $M \leqslant \sqrt{2}$ for the existence of the Kelvin–Helmholtz instability obtained by Landau (1944) with a discontinuous model. These discrepancies were solved later by Blumen, Drazin & Billings (1975) who found a new weakly unstable mode allowing the marginal stability curve to be continued up to $M = \sqrt{2}$. Besides, they also discovered new families of supersonic modes which can be unstable for large M. Similar unstable modes are also present in compressible bidimensional jets for high Mach numbers (Mack 1990) and in supersonic boundary layers (Mack 1984). The main difference is that for boundary-layer profiles, the shear-layer instability is no longer present but related modes appear for real density profiles, that Mack called inflectional instabilities.

The case of compressible round jets was considered more recently. Tam & Hu (1989) have analysed the spatial development of the instability and have proposed a classification of the different modes. A more recent numerical analysis has been performed by Luo & Sandham (1996) who also obtained different types of modes.

As in these two studies, the spatial development of the jet is not considered, and a parallel approach is used. This simplification is justified by the experimental observations which show that the mixing of the jet takes about 10 diameters, and in this region the centreline Mach number roughly remains constant (Lau 1981; Troutt & McLaughlin 1982). However, instead of performing a spatial stability analysis, we shall consider the temporal stability properties. The theory will be presented in a general context with arbitrary velocity and temperature profiles. It will be validated by comparing the theory with numerical results obtained for specific profiles.

This paper is organised as follows. In § 2, the base flow which is used in the simulation is presented and the stability equations are provided. In § 3, numerical results are obtained and compared with previous results available in the literature. The numerical results are used to identify the main characteristics of the different modes which are analysed in § 4. The framework of the theory, which is based on a large axial wavenumber WKBJ approach, is described first. Then, the three families of modes are analysed according to their asymptotic structure which is shown to depend on the locations of the turning and critical points. General predictions for the phase velocity and spatial structure of the modes are obtained and compared with the numerical results of § 3. The case of hypersonic jets for which a specific asymptotic analysis has to be performed is also considered in this section. Applications of the results to jet-noise reduction are discussed in § 5 and a brief conclusion is provided in § 6.

2. Formulation of the problem

We consider a compressible non-viscous non-conductive axisymmetric jet characterized by its velocity field $(0, 0, W(r))$, pressure $p(r)$, density $\rho(r)$ and temperature $T(r)$ where r is the radial cylindrical coordinate. The dynamics of the jet is governed by the system of equations composed of the continuity equation, the Euler equations, the energy equation and the ideal gas law.

The different variables are non-dimensionalised by using the jet radius a and the values of the axial velocity, temperature and density at the axis (W_0, T_0 and $\rho_0 = p_0/(R_g T_0)$, with R_g being the specific gas constant). Once done, the only non-dimensional parameter will be the Mach number, defined as the ratio at the axis of the jet speed with respect to the sound speed $c_0 = \sqrt{\gamma R_g T_0}$ where γ is the ratio of specific heats,

$$M = \frac{W_0}{\sqrt{\gamma R_g T_0}}. \tag{2.1}$$

For the numerical study performed in § 3, we shall use an hyperbolic tangent profile for the base-flow axial velocity

$$W(r) = \frac{W_r}{2}\left(1 + \tanh\left(\frac{R_z}{2}(1-r)\right)\right) + W_\infty, \quad W_r = 2(1-W_\infty)\left(1+\tanh\left(\frac{R_z}{2}\right)\right)^{-1}, \tag{2.2}$$

and the Crocco–Busemann relation for the temperature

$$T(r) = M^2\frac{\gamma-1}{2}(W(1+W_\infty) - W^2 - W_\infty) + T_\infty\frac{1-W}{1-W_\infty} + \frac{W-W_\infty}{1-W_\infty}, \tag{2.3}$$

where R_z is a parameter that characterizes the momentum thickness, W_∞ and T_∞ correspond to the non-dimensional velocity and temperature at infinity, respectively. Below, we shall use in most simulations the parameters $R_z = 10$, $W_\infty = 0$ and $T_\infty = 1$, that correspond to the case of an ambient jet. Note that we here apply the two-dimensional Crocco–Busemann relation to a cylindrical configuration to be able to compare our results to those of Luo & Sandham (1996). In reality, the correct relation between $T(r)$ and $W(r)$ should be obtained by numerical integration (see Duck 1990). The pressure of the base flow is assumed uniform and its density deduced from T by the ideal gas law ($\rho = 1/T$).

The theory presented in § 4 will not be limited to hyperbolic tangent profiles. General formulas will be derived for arbitrary profiles $W(r)$ and $T(r)$. These profiles would have to exhibit a particular critical point and turning point structure which will be defined below. Typically, the velocity profile would have to be a monotonically decreasing function of the radial coordinate that goes to zero at infinity.

We shall consider linear perturbations in the form of normal modes

$$(\overline{\rho}, \overline{v}, \overline{p}, \overline{T}) = (\tilde{\rho}, \tilde{u}, \tilde{v}, \tilde{w}, \tilde{p}, \tilde{T})\,\mathrm{e}^{\mathrm{i}kz+\mathrm{i}m\theta-\mathrm{i}\omega t}, \tag{2.4}$$

where k and m are the axial and azimuthal wavenumbers, respectively, and ω is the complex frequency. The equations for the perturbations are then

$$\mathrm{i}k\Phi\tilde{u} = -\frac{\tilde{p}'}{\rho}, \tag{2.5}$$

$$\mathrm{i}k\Phi\tilde{v} = -\frac{\mathrm{i}m\tilde{p}}{r\rho}, \tag{2.6}$$

$$\mathrm{i}k\Phi\tilde{w} + W'\tilde{u} = -\frac{\mathrm{i}k\tilde{p}}{\rho}, \tag{2.7}$$

$$\mathrm{i}k\Phi M^2\tilde{p} = -p\left(\frac{\partial\tilde{u}}{\partial r} + \frac{\tilde{u}}{r} + \frac{\mathrm{i}m}{r}\tilde{v} + \mathrm{i}k\tilde{w}\right), \tag{2.8}$$

where $\Phi(r) \equiv -s + W(r)$, $s = \omega/k$, and a prime denotes differentiation with respect to r.

Equations (2.5)–(2.8) can be reduced to a single equation for the pressure $\tilde{p}$ (see Tam & Hu 1989; Luo & Sandham 1996):

$$\frac{\mathrm{d}^2\tilde{p}}{\mathrm{d}r^2}+\left(\frac{1}{r}-\frac{\rho'}{\rho}-2\frac{\Phi'}{\Phi}\right)\frac{\mathrm{d}\tilde{p}}{\mathrm{d}r}+\left(k^2\beta^2(r)-\frac{m^2}{r^2}\right)\tilde{p}=0, \tag{2.9}$$

with

$$\beta^2(r)=\frac{M^2\Phi^2}{c^2}-1, \tag{2.10}$$

where $c=\sqrt{T}$, the normalized speed of sound.

The phase velocity of the perturbation is defined by $s_r=\mathrm{Re}(s)$ and its growth rate by $\omega_i=\mathrm{Im}(\omega)$.

3. Numerical results

The numerical results presented in this section have been obtained by two different methods. The first method uses a Chebyshev-spectral-collocation code similar to the one developed by Fabre & Jacquin (2004) for the incompressible Navier–Stokes equations. This code makes use of the parity properties of odd and even azimuthal modes to solve the regular singularity on the axis. A complex mapping from the Chebyshev domain $\xi \in [-1, 1]$:

$$r=\eta\frac{\xi}{\sqrt{1-\xi^2}}\,\mathrm{e}^{\mathrm{i}\theta}, \tag{3.1}$$

has also been implemented to improve the resolution of the radiative modes. The benefit of such a mapping has been discussed in detail in Riedinger, Le Dizès & Meunier (2010). Typically, we have chosen $\eta=20$ and $\theta=\pi/30$ and used $N=150$ polynomials.

The second method is a shooting method that tries to match the two solutions obtained by integrating (2.9) from 0 and from $+\infty$ with the appropriate behaviours: $\tilde{p}\sim c_0\,J_m(k\beta_0 r)$ as $r\rightarrow 0$ and $\tilde{p}\sim c_1\,K_m(k\beta_\infty r)$ as $r\rightarrow +\infty$. Both codes have been compared and validated with the results of Luo & Sandham (1996). The good agreement with the theory shown below will also confirm the accuracy of the numerical results.

In figure 1, the numerical results obtained for $m=0, 1$ and $M=3$ are displayed. In figure 1(a, c), the phase velocity of the different modes as a function of the axial wavenumber is shown. The dotted horizontal lines delimit the phase velocity intervals in which the modes share the same properties. In particular, the phase velocity limits at $s_r=-1/M, 0, 1/M$ and 1 correspond to specific convective Mach numbers $M_c=Ms_r$ which define the subsonic or supersonic character of the waves. As proposed by Tam & Hu (1989) for the vortex sheet model, four different categories can be defined as follows.

(i) Counterflow waves, $s_r\in[-1/M, 0]$: they are neutral subsonic waves travelling upstream.

(ii) Subsonic coflow waves, $s_r\in[0, 1/M]$: they are unstable subsonic waves travelling downstream.

(iii) Supersonic coflow waves, $s_r\in[1/M, 1-1/M]$: they are unstable waves travelling downstream at supersonic convective Mach numbers. They exist for $M\geqslant 2$ only.

(iv) Kelvin–Helmholtz waves, $s_r\in[0, 1]$: they are coflow waves travelling roughly at the speed of the jet in the shear region. They can be either subsonic or supersonic.

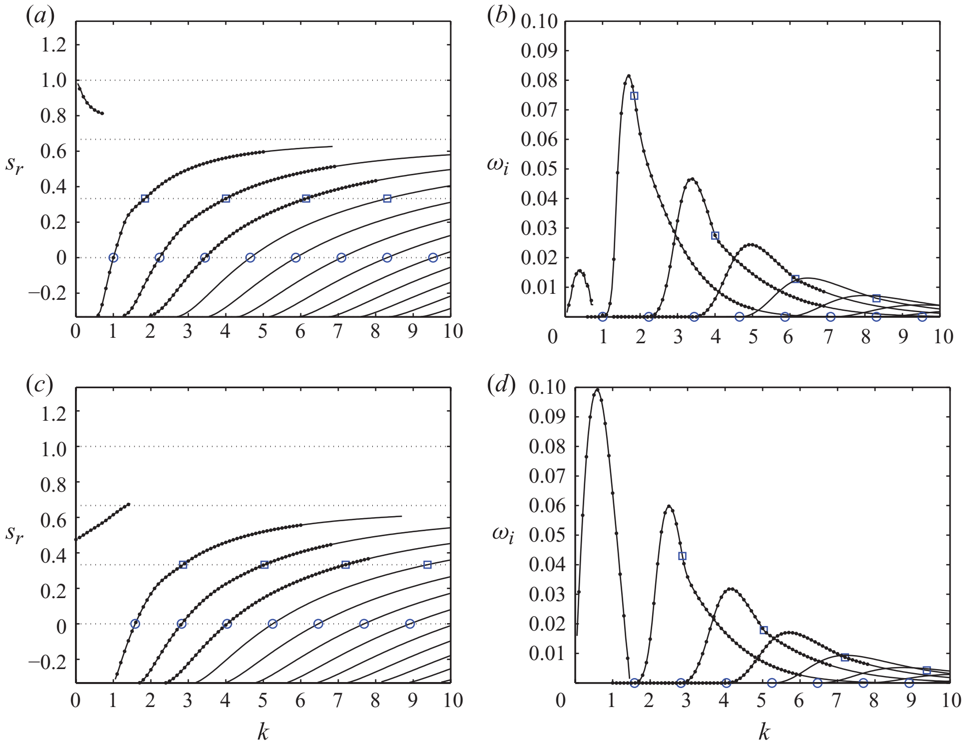

FIGURE 1. (Colour online) Numerical results. Phase velocity s_r (*a*) and (*c*) and growth rate ω_i (*b*) and (*d*) with respect to the axial wavenumber k for $M = 3$ and $m = 0$ (upper plots) and for $M = 3$ and $m = 1$ (lower plots). Solid lines: collocation results; small black dots: shooting results (only the Kelvin–Helmholtz mode and the first three branches).

The Kelvin–Helmholtz modes are special because they are formed of a single branch for each m which exists only for small axial wavenumbers. Their properties have been analysed by Batchelor & Gill (1962) for incompressible round jets and by Tam & Hu (1989) for compressible round jets. For all the other modes, there are infinitely many branches and there is no wavenumber upper bound. Each branch spans different types of modes as k increases, and its convective Mach number increases from $-1/M$ to $1 - 1/M$. In figure 1, the transition from counterflow waves to subsonic waves is indicated by a circle (○) and the transition from subsonic waves to supersonic waves by a square (□). It can be seen that all counterflow waves are neutral whereas both subsonic and supersonic coflow waves are amplified. The change from subsonic to supersonic waves is also visible in figure 1(b, d) as it corresponds to the (weak) change of slope in the growth rate curves. For the Mach number considered in figure 1, the most unstable modes are subsonic. This property seems to be always satisfied for large k. However, we shall see below that for larger Mach numbers, small wavenumber supersonic modes can also be the most unstable. The results shown in figure 1 for $m = 0$ and $m = 1$ exhibit the same trends except for the Kelvin–Helmholtz mode. As already proposed by Batchelor & Gill (1962) and Tam & Hu (1989), when $k \rightarrow 0$, the phase velocity of the Kelvin–Helmholtz mode is $s_r = 1$ for $m = 0$, but $s_r = 1/2$ for $m \neq 0$. We can also notice that the Kelvin–Helmholtz mode is more unstable for $m = 1$ than for $m = 0$. This is an effect of the Mach number, which is more clearly visible in figure 2. In figure 2, the growth rate contours are displayed in the (M, k)

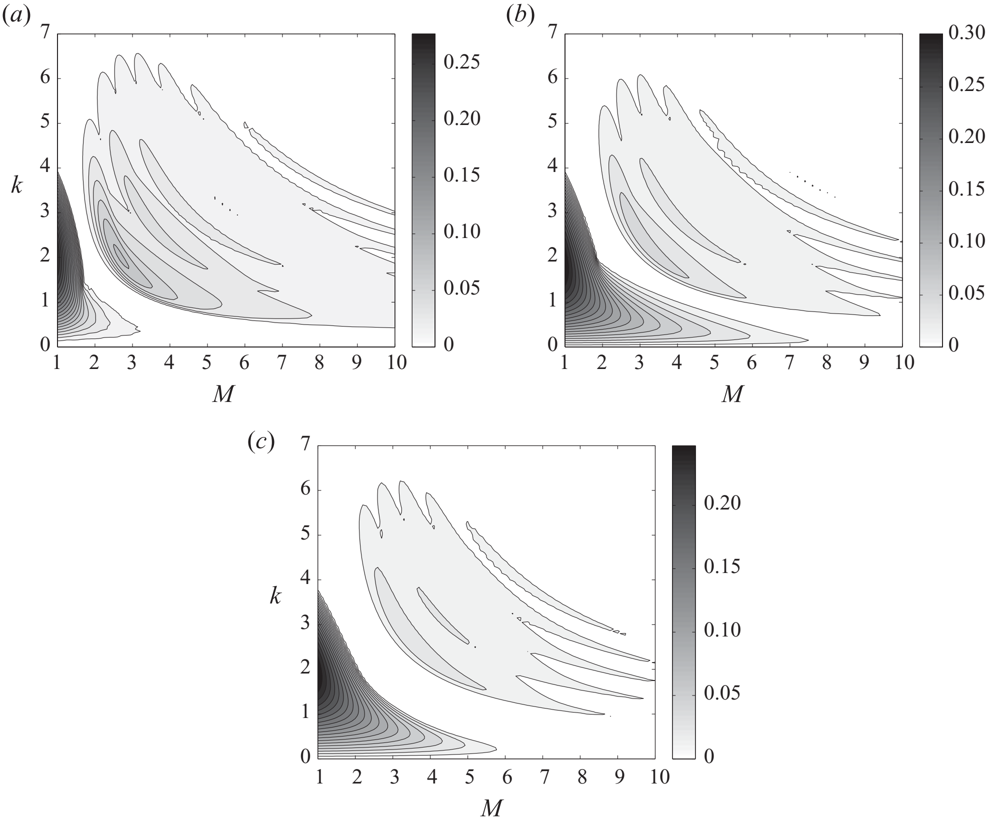

FIGURE 2. Maximum growth rate contour plot for different Mach numbers and axial wavenumbers for $m = 0$ (a), $m = 1$ (b) and $m = 2$ (c).

plane for $m = 0$, 1 and 2. For $m = 0$ (figure 2a), the Kelvin–Helmholtz mode is the only unstable mode up to $M = 1.75$, then it becomes less unstable than another mode for $M = 1.97$. Other modes also appear for larger M but they are less and less unstable. However, none of these modes become stable as M increases. This case was already pointed out by Blumen *et al.* (1975) who showed that the Kelvin–Helmholtz mode in two-dimensional mode remains unstable for all Mach numbers. For $m = 1$ and $m = 2$ (figure 2b, c) and higher azimuthal wavenumbers, the same trend is observed. The main difference is that the Kelvin–Helmholtz mode tends to be the most unstable mode up to larger values of M ($M = 5.99$ for $m = 1$ and to $M = 4.612$ for $m = 2$).

The characteristics of the most unstable mode (over all k) as a function of M are displayed in figure 3 for $m = 0, 1$ and 2. The changes of modes are clearly visible on the plots of the phase velocity and wavenumber of the most dangerous mode (figure 3b, c). We can also observe in figure 3(a) the global decreasing tendency of the maximum growth rate with respect to M. In figure 3(b), we have also plotted the curve $s_r = 1/M$ (in thick line) which is the lower limit of the region where the modes are supersonic, and therefore, emit sound. We can notice that the phase velocity of the Kelvin–Helmholtz modes becomes supersonic for M above a critical value which is $M = 1.575$ for $m = 0$, $M = 1.811$ for $m = 1$ and $M = 2.015$ for $m = 2$. For $m = 0$, a peculiar phenomenon is observed: the most unstable mode is first a subsonic Kelvin–Helmholtz mode for $M < 1.575$, then a supersonic Kelvin–Helmholtz mode

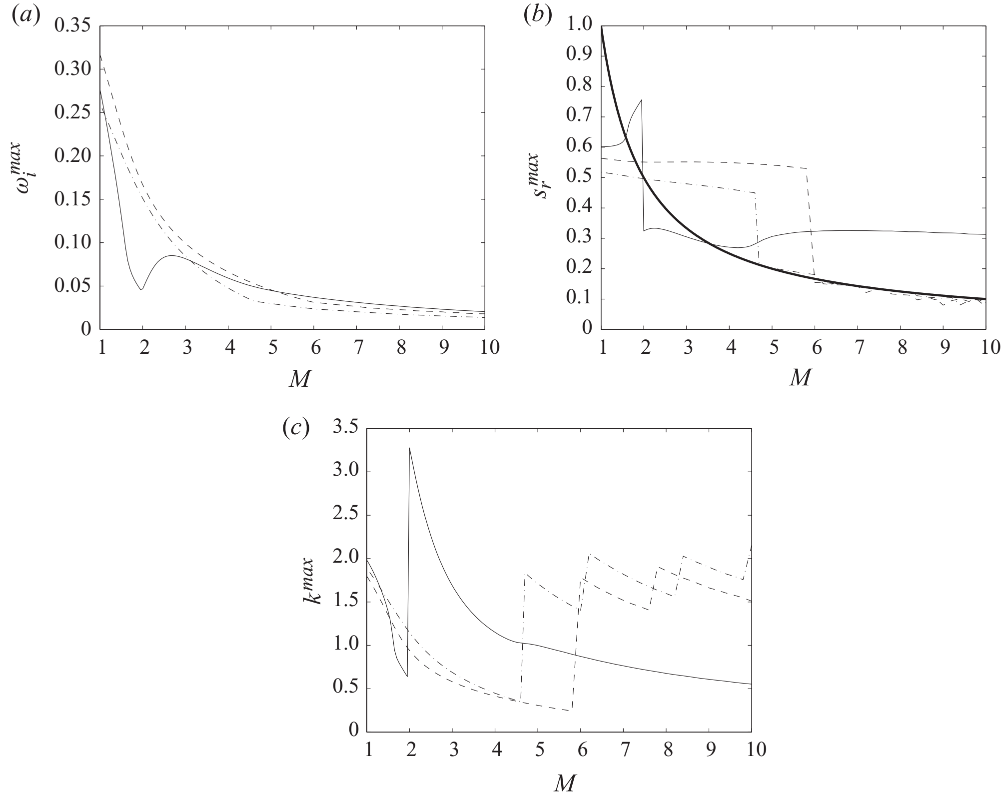

FIGURE 3. Characteristics of the most unstable mode (over all k) versus M for $m = 0$ (solid line), $m = 1$ (dashed line) and $m = 2$ (dash-dotted line). (*a*) Maximum growth rate. (*b*) Phase velocity of the most unstable mode. (*c*) Axial wavenumber of the most unstable mode. The thick solid line (defined by $s_r = 1/M$) is the lower limit of the region where the phase velocity is supersonic, that is the most unstable mode radiating.

up to $M = 1.97$, then a subsonic coflow wave up to $M = 3.541$, and thereafter a supersonic wave. Thus, the most unstable axisymmetric mode does not emit sound in the Mach interval (1.97, 3.541). For $m = 1$ and $m = 2$, the Kelvin–Helmholtz mode is also dominant for small Mach numbers, then the most unstable mode becomes a coflow mode which remains close to transonic ($s_r \approx 1/M$).

In the following section, we build an asymptotic theory to describe counterflow and coflow waves. Particular attention is paid to the supersonic waves which are responsible for sound emission and become the most unstable modes for $M \gtrsim 5$. The Kelvin–Helmholtz modes, which are relevant for smaller Mach numbers will not be considered. Their properties have been discussed in Tam & Hu (1989).

4. Asymptotic descriptions of the modes

In this section, we shall see how a theoretical analysis can be used to associate with each type of mode a specific spatial structure. The theory is based on a WKBJ asymptotic analysis in the limit of large axial wavenumber. The method, which was first introduced in the quantum mechanics framework, is described in Bender & Orszag (1999). It has already been used to describe normal modes in homogeneous vortices (Le Dizès & Lacaze 2005) and in stratified vortices (Le Dizès 2008; Le Dizès &

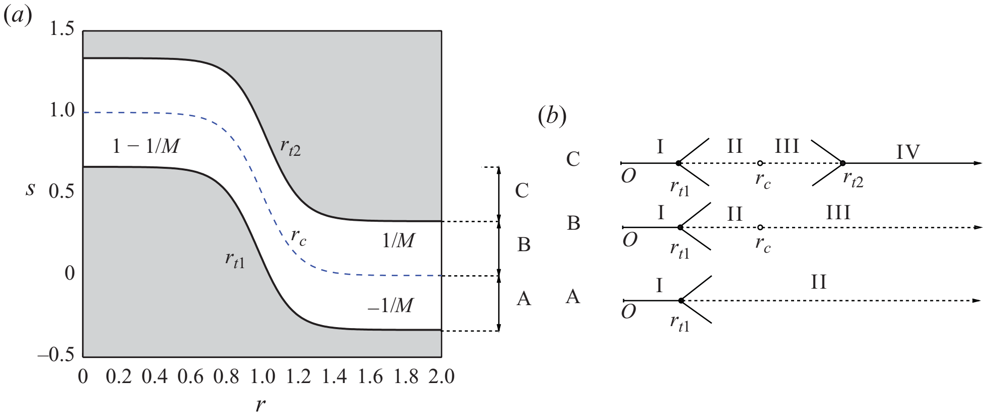

FIGURE 4. (Colour online) (*a*) Sign of the radial wavenumber β^2. The shadowed zone corresponds to $\beta^2 > 0$. Each turning point is marked by thick lines and the critical point by a dashed line (both s and r are assumed real in this plot). (*b*) Sketch of the different radial structures of the modes. On the solid line, the solution is oscillating and on the dashed line it is damped. Also each turning point is marked with a solid circle and is shown with its Stokes lines. Open circles are critical points.

Billant 2009). Here, we shall first assume that $k \gg M > 1$. The case where both k and M are large and of same order is considered afterwards.

The pressure is sought in the form of a WKBJ expansion:

$$p(r) = \left(p_0(r) + \frac{p_1(r)}{k} + \cdots \right) \mathrm{e}^{k\phi(r)}. \tag{4.1}$$

By plugging this expression in (2.9), we obtain at leading order (in $1/k$)

$$\phi(r) = \pm \mathrm{i} \int^r \beta(r), \tag{4.2}$$

and, at the next order, a differential equation for the amplitude $p_0(r)$ whose solution is

$$p_0(r) = A \left| \frac{\rho \Phi^2}{r\beta} \right|^{1/2}, \tag{4.3}$$

where A is an arbitrary constant that we shall fix to unity. The above expressions define approximations of two independent solutions in regions where β^2 does not change sign. The approximations break down around the points where β vanishes. These so-called turning points satisfy $(s - W(r_t))^2 = c^2/M^2$. Turning points delimit intervals in which the solutions are oscillating (if $\beta^2 > 0$) or exponential (if $\beta^2 < 0$). In this study, there exist, for each phase velocity s, at most, two turning points r_{t_1} and r_{t_2}, and the solutions are exponential between the two turning points. Figure 4(*a*) shows the variation of r_{t_1} and r_{t_2} versus s for $M = 3$ for the hyperbolic tangent profile.

The location of the critical point r_c which satisfies $s = W(r_c)$ is also indicated in this figure. This point is a singularity of the Euler equations. Contrarily to the case of vortices (see Le Dizès & Lacaze 2005), this singularity is *a priori* regular for a jet. However, as we shall see below, it modifies the WKBJ approximations and is responsible for the destabilization of the modes. In figure 4(*a*), turning points and the critical point are real because s is assumed real. In the unstable cases, s is (slightly) complex and these points slightly move in the complex plane. However, we shall see that in those cases a good approximation of the mode structure is obtained by assuming s real at leading order.

According to the value of s, different radial structures are obtained. When s is larger than $1 + 1/M$ or more negative than $-1/M$, β^2 is everywhere positive: the solutions are then oscillating everywhere and no mode can be formed because the condition of radiation forbids the inward propagating wave. As explained by Le Dizès & Lacaze (2005) and Le Dizès & Billant (2009), normal modes are expected when there is a finite interval in r in which the solutions are oscillating. This interval plays the role of the potential hole of quantum mechanics and modes can be formed if there is a discretized number of radial oscillations in this interval. In this case, there exists a finite interval where β^2 is positive when $s \in (-1/M, 1-1/M)$. However, three different radial structures can be obtained which correspond to the different modes defined in § 3. As illustrated in figure 4(*b*), for all modes there is a region $(0, r_{t1})$ in which the solutions exhibit an oscillating behaviour. For counterflow modes (case A: $s \in [-1/M, 0]$), the solution is evanescent outside. For subsonic coflow modes (case B: $s \in [0, \min(1/M, 1 - 1/M)]$), the structure is similar except that there is a critical point in the evanescent domain (r_{t1}, ∞). For supersonic coflow modes (case C: $s \in [1/M, 1 - 1/M]$), there is an additional region after a second turning point r_{t2} in which the solution is oscillatory. As mentioned above, these modes exist only if $M > 2$.

In the following, we provide, using the WKBJ approach, the spatial structure and the dispersion relation of each type of eigenmode. Formulas will be obtained for arbitrary profiles $W(r)$ and $T(r)$. However, this will implicitly assume that the modes have the critical and turning point structure shown in figure 4(*b*). For an ambient jet with the Crocco–Buseman relation (2.3) for the temperature, this will be the case for any monotonically decreasing velocity profile that vanishes at infinity. But more general temperature and velocity profiles could *a priori* be used as long as the critical and turning point structure is as in figure 4(*b*).

The principle of the analysis is to solve the asymptotic problem in the different regions and to obtain the dispersion relation as a condition of matching of the different solutions. To facilitate the reading, we shall consider here only the WKBJ approximations. The solutions close to the turning point or close to the critical point are provided in the Appendix. It is from the local analysis near those points that the transition formula from one WKBJ approximation valid on one side to another valid on the other side can be obtained.

Using the formalism developed in Shepard (1983), we introduce the notations

$$u(c, r) = \left| k \int_c^r \beta_r \, \mathrm{d}r \right|, \tag{4.4a}$$

$$v(c, r) = \left| k \int_c^r \beta_i \, \mathrm{d}r \right|, \tag{4.4b}$$

for the phase of the WKBJ approximations in oscillating and exponential regions, respectively. General expressions of WKBJ approximations can then be written as

$$p(r) \sim p_0(r)(A^+ \exp(\mathrm{i}u(c, r)) + A^- \exp(-\mathrm{i}u(c, r))), \tag{4.5a}$$

$$p(r) \sim p_0(r)(A^+ \exp(v(c, r)) + A^- \exp(-v(c, r))) \tag{4.5b}$$

in oscillating regions and in exponential regions, respectively, where $p_0(r)$ is given by (4.3).

As already mentioned above, WKBJ approximations are valid as long as we are far from a singularity. The connection formulas which link the approximations on each side of a singularity (that is the relation between the coefficient $A^{\pm}$ on either side of the singularity) are obtained by a local analysis of the singular point.

For a turning point, the result is classical and has been used in several places (see Shepard 1983). For completeness, it is briefly reproduced in the Appendix. If we stay on the real axis (where the solutions are purely oscillating or pure exponential), we obtain the following reversible connection formulas:

$$2\sin(u(r_t, r) + \pi/4) \longleftrightarrow \mathrm{e}^{-v(r_t,r)}, \tag{4.6a}$$

$$\cos(u(r_t, r) + \pi/4) \longleftrightarrow \mathrm{e}^{v(r_t,r)}. \tag{4.6b}$$

These relations have to be interpreted as follows: if, for instance, on one side of the turning point, the solution is given by (4.5*b*) with $A^+ = 1$ and $A^- = 0$, (4.6*b*) implies that, on the other side, the solution is given by (4.5*a*) with $A^{\pm} = (1 \pm \mathrm{i})/(2\sqrt{2})$. Moreover, the relations are reversible and the exponential side can be either on the right or on the left of the turning point.

If the singularity is a critical point, different relations, which are derived in the Appendix are obtained

$$\mathrm{e}^{-v(r_c,r)} \longleftrightarrow -\mathrm{e}^{v(r_c,r)} + \frac{L\pi\mathrm{i}}{2k}\,\mathrm{e}^{-v(r_c,r)}, \tag{4.7a}$$

$$\mathrm{e}^{v(r_c,r)} \longleftrightarrow \frac{L\pi\mathrm{i}}{2k}\,\mathrm{e}^{v(r_c,r)} - \left(1 - \frac{L\pi^2}{4k^2}\right)\mathrm{e}^{-v(r_c,r)}, \tag{4.7b}$$

with

$$L = \frac{1}{r_c} - \frac{\rho_c'}{\rho_c} - \frac{W_c''}{2W_c'}, \tag{4.8}$$

where the index c means values taken at r_c. Contrarily to the previous formulas, these relations are not reversible.

For convenience, we also introduce the notation

$$U_{01} = u(0, r_{t_1}), \tag{4.9a}$$

$$V_{1c} = v(r_{t_1}, r_c), \tag{4.9b}$$

$$V_{c2} = v(r_c, r_{t_2}). \tag{4.9c}$$

4.1. *Counterflow modes*

Counterflow modes have a simple structure, as there are two different regions only (see figure 4*b* for case A). In the oscillating region (region I), the condition of matching with the local solution that is regular at the origin (see Appendix where this solution is obtained) imposes that the solution must be written as

$$p_I(r) = p_0(r)\cos\left(u(0, r) - \frac{|m|\pi}{2} - \frac{\pi}{4}\right). \tag{4.10}$$

This expression can also be written as

$$p_I(r) = p_0(r)\left(\sin\left(U_{01} - |m|\frac{\pi}{2}\right)\sin\left(u(r_{t_1}, r) + \frac{\pi}{4}\right)\right.$$
$$\left. + \cos\left(U_{01} - |m|\frac{\pi}{2}\right)\cos\left(u(r_{t_1}, r) + \frac{\pi}{4}\right)\right). \tag{4.11}$$

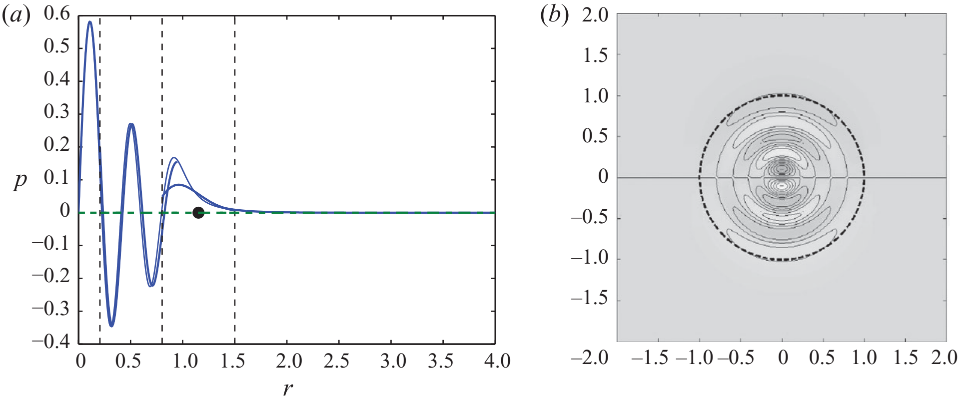

FIGURE 5. (Colour online) (*a*) Pressure amplitude (solid lines: real part; dashed lines: imaginary part) of a counterflow mode for $M=3$, $m=1$, $s=-0.1954$ and $k=5$. Thick lines are asymptotic approximations for the same parameters except $k=4.8566$, thin lines are the numerical solution. The different regions of the asymptotical analysis are indicated by vertical lines. (*b*) Structure of the numerical solution in the (x, y) plane for the same parameters.

Using the connection formulas (4.6*a*, *b*), we can deduce the WKBJ approximation in region II:

$$p_{II}(r)=\frac{p_0(r)}{2}\left(\frac{1}{2}\sin\left(U_{01}-|m|\frac{\pi}{2}\right)\mathrm{e}^{-v(r_{t_1},r)}+\cos\left(U_{01}-|m|\frac{\pi}{2}\right)\mathrm{e}^{v(r_{t_1},r)}\right). \qquad (4.12)$$

In region II, only decaying solutions are allowed, so the term multiplying the growing part of the solution p_{II} has to be zero ($\cos(U_{01}-|m|\pi/2)=0$). This provides the dispersion relation

$$k\int_0^{r_{t1}}\beta\,\mathrm{d}r=\frac{|m|\pi}{2}+\frac{\pi}{2}+n\pi, \qquad (4.13)$$

where n is an integer. The above condition is a condition of discretization of the number of radial oscillations of the solution in region I. For a fixed phase velocity $s\in(-1/M,0)$, it leads to a discrete number of axial wavelengths. These modes are purely neutral and are the exact analogue of the neutral Kelvin modes of a vortex as described by Le Dizès & Lacaze (2005). Also note that the above formula is the extension to three-dimensional modes of the results obtained by Mack (1990) in two-dimensional shear flows.

In figure 5, the radial structure of a counterflow mode is shown for $M=3$, $m=1$, $s=-0.1954$ and $k=5$. This numerical solution is compared with the asymptotic solution obtained in different regions (delimited by the vertical dashed lines) for the axial wavenumber $k=4.8566$ deduced from (4.13) for $n=4$. As can be noticed, the agreement between the theory and the numeric is good. Other comparisons have been performed leading to the same conclusion. The dispersion relation which will be compared with the numerical results in § 6 will be shown to provide a good approximation.

4.2. *Subsonic coflow modes*

The structures of these modes are similar to counterflow modes in regions I and II. However, owing to the presence of a critical point, a third region III where WKBJ approximations are different has to be considered. The approximation (4.12) of the solution in region II can be written as

$$p_{II}(r) = \frac{p_0(r)}{2}\left(\frac{1}{2}\sin\left(U_{01} - |m|\frac{\pi}{2}\right)\mathrm{e}^{-V_{1c}+v(r_c,r)} + \cos\left(U_{01} - |m|\frac{\pi}{2}\right)\mathrm{e}^{V_{1c}-v(r_c,r)}\right). \tag{4.14}$$

Applying the connection formula (4.7), we deduce the approximation in region III:

$$p_{III}(r) = p_0(r)\left(A^+_{III}\,\mathrm{e}^{v(r_c,r)} + A^-_{III}\,\mathrm{e}^{-v(r_c,r)}\right), \tag{4.15}$$

with

$$A^+_{III} = \frac{1}{2}\sin(U_{01} - |m|\pi/2)\frac{L\pi\mathrm{i}}{2k}\,\mathrm{e}^{-V_{1c}} - \cos(U_{01} - |m|\pi/2)\,\mathrm{e}^{V_{1c}}, \tag{4.16a}$$

$$A^-_{III} = \frac{L\pi\mathrm{i}}{2k}\cos(U_{01} - |m|\pi/2)\,\mathrm{e}^{V_{1c}} - \frac{1}{2}\sin(U_{01} - |m|\pi/2)\,\mathrm{e}^{-V_{1c}}\left(1 - \frac{L^2\pi^2}{4k^2}\right). \tag{4.16b}$$

The dispersion relation is obtained by requiring the dominant solution to vanish, that is $A^+_{III} = 0$. This yields the condition

$$k\int_0^{r_{t1}} \beta\,\mathrm{d}r = n\pi + \frac{|m|\pi}{2} + \pi/2 - \frac{\mathrm{i}\pi L}{4k}\exp\left(-2k\int_{r_{t_1}}^{r_c}|\beta|\,\mathrm{d}r\right). \tag{4.17}$$

This condition resembles the previous condition obtained for the counterflow modes. The additional complex term is responsible for a frequency correction which can be calculated by expanding the phase velocity as $s = s_0 + s_1\mathrm{i}$, with $|s_0| \gg |s_1|$. We then obtain at leading order expression (4.13), and at the next order

$$\omega_i = s_1 k = \frac{-L\pi\exp\left(-2k\displaystyle\int_{r_{t_1}}^{r_c}|\beta|\,\mathrm{d}r\right)}{4k\displaystyle\int_0^{r_{t_1}}\left.\frac{\mathrm{d}\beta}{\mathrm{d}s}\right|_{s=s_0}\mathrm{d}r}, \tag{4.18}$$

where we recall that L is given by (4.8).

This expression is positive because L is positive (see figure 7*a*) and $\mathrm{d}\beta/\mathrm{d}s$ is negative. Subsonic coflow modes are, therefore, slightly unstable with a growth rate ω_i given by (4.18). This result is qualitatively in agreement with the numerical results discussed in § 3. Quantitative comparisons are made in § 6.

In figure 6, the pressure amplitude of the numerical eigenmode for $M = 3$, $m = 1$ and $k = 8.75$ is presented. For this case, there is a weak amplification: $s \approx 0.195 + 5.96 \times 10^{-4}\mathrm{i}$. For the same real part of the phase velocity, the analytical prediction gives an axial wavenumber $k = 8.444$ and a complex phase velocity $s = 0.195 + 7.33 \times 10^{-4}\mathrm{i}$, which is in relatively good agreement with the numeric. The asymptotic structure obtained for these values has also been plotted in figure 6. We can see that it correctly captures the spatial structure of the mode.

We would like to mention that Tam & Hu (1989) had already observed some of the characteristics mentioned here. First, they showed that only coflow modes can become unstable among all subsonic modes. They demonstrated the continuity of the branches and identified one of the main differences between coflow and counterflow modes: the presence of a critical point in their spatial structure. We have seen here that the presence of the critical point in subsonic coflow modes has a destabilizing effect in compressible jets depending on the sign of L. For the base-flow profile studied here and $M = 3$, L is indeed responsible for the destabilization. Moreover, we have obtained that the growth rate is proportional to the parameter L defined in (4.8) which depends on the characteristics of the jet at r_c.

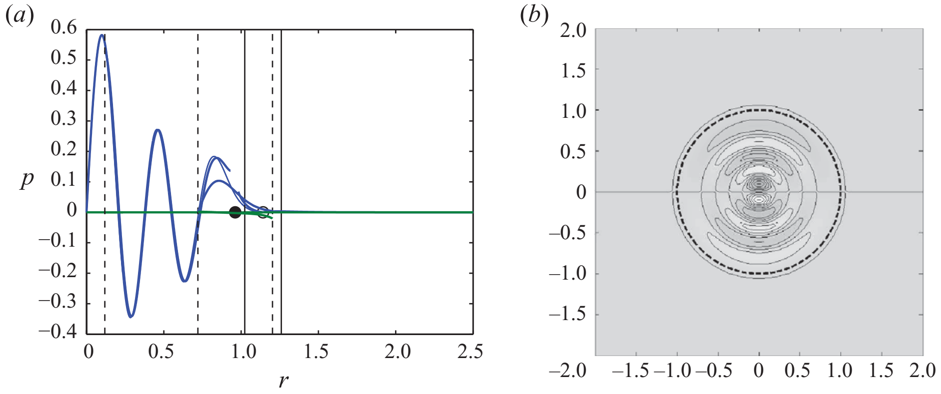

FIGURE 6. (Colour online) (*a*) Pressure amplitude (solid lines: real part; dashed lines: imaginary part) of a subsonic coflow mode for $M = 3$, $m = 1$, $s = 0.195 + 5.96 \times 10^{-4}\mathrm{i}$ and $k = 8.75$. Thick lines are asymptotic approximations for the mode obtained for the same parameters except $k = 8.444$ and $s = 0.195 + 7.33 \times 10^{-4}\mathrm{i}$, thin lines are the numerical solution. The different regions of the asymptotical analysis are indicated by vertical lines: dashed for the near axis region and the turning point region, solid for the critical point region. The imaginary part of the solution and the approximation are so small that it is difficult to see them. (*b*) Structure of the numerical solution in the (x, y) plane for the same parameters.

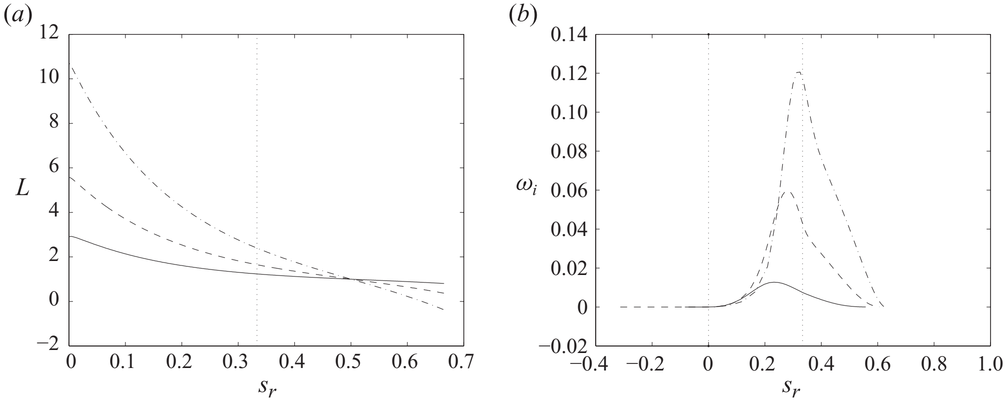

FIGURE 7. Effect of the steepness. Results for $R_z = 5$ (solid), $R_z = 10$ (dashed line) and $R_z = 20$ (dash-dotted line). (*a*) Variation of L versus s_r. (*b*) Growth rate ω_i of the first $m = 1$ mode versus s_r. The limits of the coflow subsonic region are marked by dotted lines ($s_r \in (0, 1/M)$).

In figure 7(*a*), the variations of L with respect to the phase velocity are plotted for three different jets for a given Mach number. We observe that L (for $s_r < 0.5$) tends to increase as the steepness R_z of the jet increases. The numerical results for the first $m = 1$ mode are in qualitative agreement with this tendency (for values of s_r between 0.2 and 0.4, respectively), as shown in figure 7(*b*). For smaller values of s_r, the critical point moves away from the jet in such a way that the exponential factor in (4.18) becomes the dominant contribution. This explains why for a fixed small value of s_r there is an optimal steepness which maximizes the instability as observed by Tam & Hu (1989).

However, when we consider the most unstable mode, the maximum growth rate does increase as the steepness increases.

The mechanism of the instability can be associated with a mechanism of over-reflection and is very similar to one described by Le Dizès & Billant (2009) which will apply to the supersonic modes. Indeed, the critical point modifies the condition of transmission in the evanescent domain II such that if we consider an incident wave packet in region I, it is reflected with a larger amplitude. The principle of the over-reflection mechanism has been analysed in detail in several works (Lindzen & Barker 1985) and documented in other contexts (Takehiro & Hayashi 1992).

4.3. *Supersonic coflow modes*

As soon as $s_r > 1/M$, the solutions become oscillating at infinity. An additional turning point appears in the spatial structure of the mode (see figure 4*b*) such that the solutions have to be considered in the region IV to obtain the dispersion relation. The approximations obtained for the previous modes still apply in regions I, II and III. However, in region III, we should not require A^+_{III} to vanish. The condition on the coefficients $A^\pm_{III}$ is obtained by applying the condition that the WKBJ solution in region IV is a single outward wave. To obtain this condition, it is useful to write (4.15) as

$$p_{III}(r) = p_0(r)\left(A^+_{III}\,\mathrm{e}^{V_{c2}}\,\mathrm{e}^{-v(r_{t_2},r)} + A^-_{III}\,\mathrm{e}^{-V_{c2}}\,\mathrm{e}^{v(r_{t_2},r)}\right), \tag{4.19}$$

such that we can deduce by applying the connection formulas (4.6*a*, *b*), the expression of p in region IV

$$p_{IV}(r) = p_0(r)\left(A^+_{III}\,\mathrm{e}^{V_{c2}}2\sin(u(r_{t_2},r)+\pi/4) + A^-_{III}\,\mathrm{e}^{-V_{c2}}\cos(u(r_{t_2},r)+\pi/4)\right), \tag{4.20}$$

where $A^\pm_{III}$ are given by (4.16*a*, *b*). This expression can also be written as

$$p_{IV}(r) = p_0(r)\left(A^+_{IV}\,\mathrm{e}^{\mathrm{i}u(r_{t_2},r)+\mathrm{i}\pi/4} + A^-_{IV}\,\mathrm{e}^{-\mathrm{i}u(r_{t_2},r)-\mathrm{i}\pi/4}\right), \tag{4.21}$$

with

$$A^+_{IV} = -\mathrm{i}A^+_{III}\,\mathrm{e}^{V_{c2}} + A^-_{III}\,\mathrm{e}^{-V_{c2}}/2, \tag{4.22a}$$

$$A^-_{IV} = \mathrm{i}A^+_{III}\,\mathrm{e}^{V_{c2}} + A^-_{III}\,\mathrm{e}^{-V_{c2}}/2. \tag{4.22b}$$

The condition of radiation ($A^-_{IV} = 0$) then provides the dispersion relation of the supersonic coflow modes:

$$k\int_0^{r_{t1}} \sqrt{\beta}\,\mathrm{d}r = \frac{|m|\pi}{2} + \pi/2 + n\pi - \mathrm{i}\frac{L\pi}{4k}\,\mathrm{e}^{-2V_{1c}} - \frac{\mathrm{i}}{4}\,\mathrm{e}^{-2V_{12}}. \tag{4.23}$$

As for subsonic modes, we can deduce, by expanding $s = s_0 + s_1\mathrm{i}$ with $s_1 \ll 1$, at leading order

$$k = \frac{|m|\pi/2 + \pi/2 + n\pi}{\displaystyle\int_0^{r_{t_1}(s_0)} |\beta(s_0)|\,\mathrm{d}r}, \tag{4.24}$$

and at the next order

$$\omega_i = s_1\,k = -\frac{\dfrac{L\pi}{k}\,\mathrm{e}^{-2V_{1c}} + \mathrm{e}^{-2V_{12}}}{4\displaystyle\int_0^{r_{t_1}(s_0)} \left.\frac{\mathrm{d}\beta}{\mathrm{d}s}\right|_{s=s_0}\mathrm{d}r}. \tag{4.25}$$

In the above expression, we clearly see the contribution from the critical point (the first term) which is the same as for the subsonic modes and the contribution from the second turning point associated with acoustic emission (the second term). Whereas the critical point contribution can *a priori* be either stabilizing or destabilizing (according to the sign of L), the radiation contribution is always destabilizing. A very similar expression was obtained by Le Dizès & Billant (2009) for the radiative mode

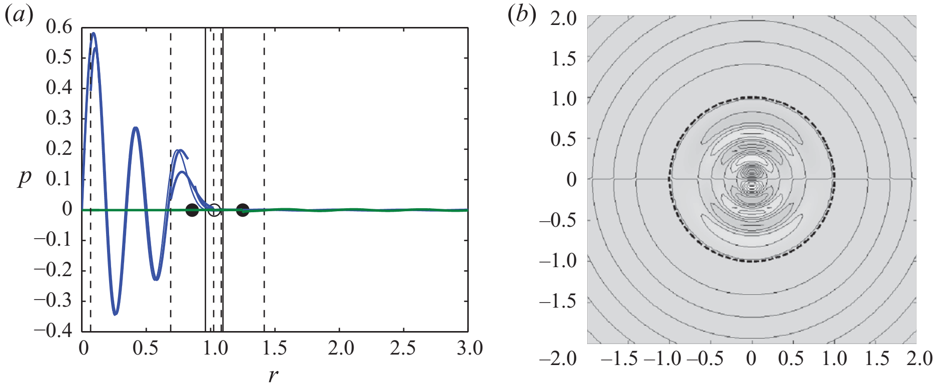

FIGURE 8. (Colour online) (*a*) Pressure amplitude (solid lines: real part; dashed lines: imaginary part) of a supersonic coflow mode for $M = 3$, $m = 1$, $s = 0.4293 + 2.855 \times 10^{-5}\mathrm{i}$ and $k = 15$. Thick lines are asymptotic approximations for the mode obtained for the same parameters except $k = 14.673$ and $s = 0.4293 + 2.859 \times 10^{-5}\mathrm{i}$, thin lines are the numerical solution. The different regions of the asymptotical analysis are indicated by vertical lines: dashed for the near axis region and the turning point regions, solid for the critical point region. The imaginary part of the solution and the approximation are so small that it is difficult to see them. (*b*) Structure of the numerical solution in the (x, y) plane for the same parameters.

in a stratified vortex. However, in that case, the critical point contribution was always stabilizing.

As for the two other types of modes, the WKBJ solution provides a good approximation of the eigenmodes as illustrated in figure 8.

When M becomes very large, the distances between the two turning points and the critical point which are of order $1/M$ become small. If they become smaller than $(k^{-1/2})$, the two turning points cannot be considered as separated, and therefore, the above WKBJ analysis breaks down. However, when M is of the order k, a new asymptotic analysis can be constructed as $k \to \infty$. In that case, the two turning points and the critical point are merged at leading order to a single point r_c and there exist only two regions I and IV. If $M = M_0 k$, in region I, the WKBJ approximation of the solution (which matches the local solution bounded at the origin) is now slightly different

$$p_I(r) = p_0(r) \cos\left(k^2 \int_0^r \frac{M_0 \Phi}{c}\,\mathrm{d}r - \int_0^r \frac{c}{2M_0\Phi}\,\mathrm{d}r - \frac{|m|\pi}{2} - \frac{\pi}{4}\right), \tag{4.26}$$

with

$$p_0(r) = \left|\frac{\rho\, c}{r\Phi}\right|^{1/2}. \tag{4.27}$$

This expression can also be written as

$$p_I(r) = \frac{p_0(r)}{2} \exp\left(-\mathrm{i}\tilde{u}(r_c, r) + \mathrm{i}\tilde{U}_{0c} - \mathrm{i}\frac{|m|\pi}{2} - \mathrm{i}\frac{\pi}{4}\right) + \exp\left(+\mathrm{i}\tilde{u}(r_c, r) - \mathrm{i}\tilde{U}_{0c} + \mathrm{i}\frac{|m|\pi}{2} + \mathrm{i}\frac{\pi}{4}\right), \tag{4.28}$$

with

$$\tilde{u}(r_c, r) = k^2 \left|\int_{r_c}^r \frac{M_0\Phi}{c}\,\mathrm{d}r\right| - \frac{1}{2\lambda_c} \log|r - r_c|, \tag{4.29a}$$

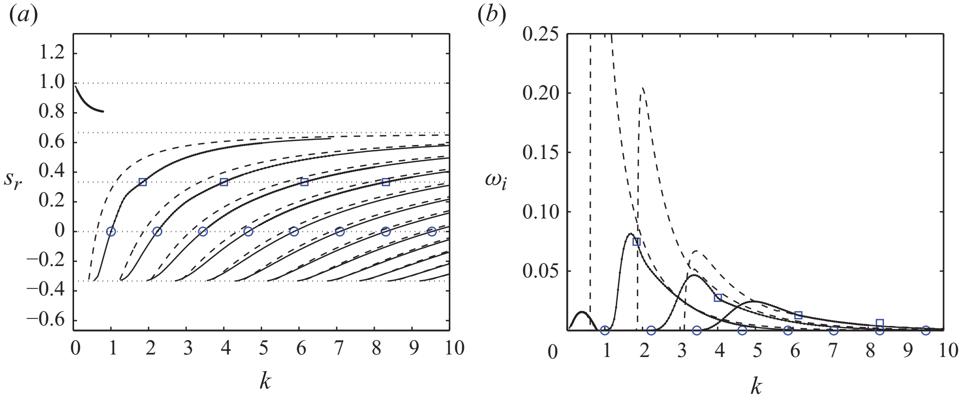

FIGURE 9. (Colour online) Comparison of the phase velocity (*a*) and growth rate (*b*) of the modes versus k for $M=3$ and $m=0$. Solid lines: numerical results; dashed lines: theoretical predictions. In (*b*), only the Kelvin–Hemholtz mode and the first three branches are shown.

$$\tilde{U}_{0c} = k^2 \int_0^{r_c} \frac{M_0 \Phi}{c}\,\mathrm{d}r - \int_0^{r_c} \left(\frac{c}{2M_0\Phi} - \frac{1}{2\lambda_c |r - r_c|} \right) \mathrm{d}r + \frac{1}{2\lambda_c} \log |r_c|, \quad (4.29b)$$

with $\lambda_c = M_0 |W_c'|/c_c$. Using the connection formulas (A 19*a*, *b*), we can deduce the condition that guarantees that only the wave propagating outwards is present after r_c in region IV

$$\mathrm{e}^{2\mathrm{i}\tilde{U}_{0c} - \mathrm{i}|m|\pi - \mathrm{i}\frac{\pi}{2}} = 2\mathrm{i}\sin(5\pi/4 - \mathrm{i}\pi/(4\lambda_c)) \frac{\Gamma(5/4 - \mathrm{i}/(4\lambda_c))}{\Gamma(5/4 + \mathrm{i}/(4\lambda_c))} \kappa^{2\mathrm{i}}, \quad (4.30)$$

with $\kappa = (\mathrm{i}\lambda_c k^2)^{1/(4\lambda_c)}$. The new dispersion relation for the supersonic coflow modes valid when $M = O(k)$ for large k can then be written as

$$\begin{aligned} \tilde{U}_{0c} = {} & \frac{|m|\pi}{2} + \frac{\pi}{2} + n\pi + \frac{\pi \mathrm{i}}{8\lambda_c} + \frac{1}{4\lambda_c} \log(\lambda_c k^2 r_c^2) \\ & - \frac{\mathrm{i}}{2} \left[\log\left(2 \sin(5\pi/4 - \mathrm{i}\pi/(4\lambda_c))\right) + \log\left(\frac{\Gamma(5/4 - \mathrm{i}/(4\lambda_c))}{\Gamma(5/4 + \mathrm{i}/(4\lambda_c))} \right) \right]. \quad (4.31) \end{aligned}$$

Note that when $M_0 \to \infty$, $\lambda_c \to \infty$ so that the last two terms reduce to $-\pi/2 - \mathrm{i}\log(2)/4$. In that case, the dispersion relation is similar to that obtained for the normal modes in a stratified vortex when the two turning points and the critical point are also merged (Le Dizès & Billant 2009).

4.4. *Comparison with numerical results*

In the previous sections, we have obtained theoretical predictions for the subsonic and supersonic modes of the jet. In this section, we want to compare these predictions with the numerical results.

Except in the hypersonic case ($M = O(k)$), for the three families of modes, we have seen that the real part of the phase velocity is related to the axial wavenumber by the same relation (4.13). This relation is compared with the numerical results obtained for $m=0$ and $M=3$ in figure 9(*a*). As can be noticed the different branches are well-captured by the theoretical dispersion relation. Moreover, the agreement improves as k increases as expected. Three different expressions for the growth rate of the modes have been obtained. Counterflow modes are neutral. Subsonic coflow modes are unstable with a growth rate given by (4.18). Supersonic coflow modes are unstable

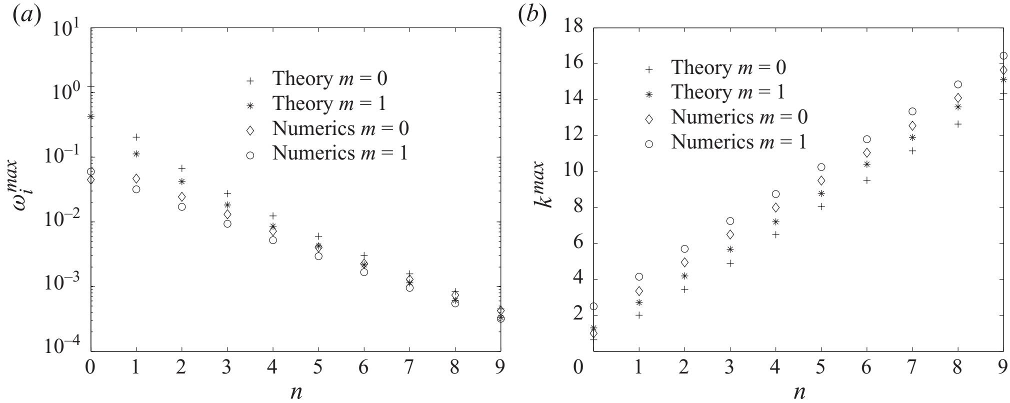

FIGURE 10. Theoretical prediction and numerical value of the maximum growth rate (a) and of the most dangerous wavenumber (b) as a function of the branch label n for $m = 0, 1$ and $M = 3$.

with a growth rate given by (4.25). Comparisons with the numeric are provided in figure 9(b). The agreement is less good than for the phase velocity, but the theory still provides the general trends of the modes. For these relatively small values of k, we are clearly at the limit of applicability of the theory. The theory does provide better estimates for larger wavenumbers, or for larger values of the label n of the branch. This can be checked in figure 10 in which we have plotted the values of the maximum growth rate and of the most dangerous wavenumber as a function of the branch label n for the two cases considered in figure 1 ($m = 0$ and $m = 1$ for $M = 3$).

It is also interesting to mention that although we are at the limit of applicability of the theory, the theory provides qualitatively the trends of instability characteristics. In particular, we have seen that the growth rate formula depends exponentially on integrals between the turning points and the critical point. As M increases, the distance between the turning points and the critical point decreases, and thus, also the integrals between these points. As a consequence, the growth rate is expected to increase as M increases. This is what has been checked in figure 11(a) for the mode $n = 4$ for $m = 0$ and $m = 1$.

For very large Mach numbers, we have obtained a different dispersion relation for supersonic modes (see (4.31)). This formula is compared to numerical results for $m = 1$ and $M = 10$ in figure 12. We can see that the agreement between theory and numeric is excellent for the phase velocity even for the first branch and small wavenumbers. In particular, note that the agreement is better than the formula derived for small M which has also been plotted in this figure. For the growth rate, the agreement is correct mainly for wavenumbers close to the Mach number. This is what we expect from the theory. Yet, for larger wavenumbers, it is difficult to know whether the theory still works because the growth rate becomes too small to be calculated numerically with a good precision.

The two formulas for supersonic modes have also been tested by fixing the relation between the Mach number and the axial wavenumber in figure 13. In this figure, the phase velocity and the growth rate of the modes obtained for $m = 0$ when $k = 3M$ and $k = M$, as M varies are compared. For $k = 3M$, which is neither very large with respect to M nor equal, both formulas provide pretty good results (for both the phase velocity and the growth rate), although for higher Mach numbers, the growth rate is better

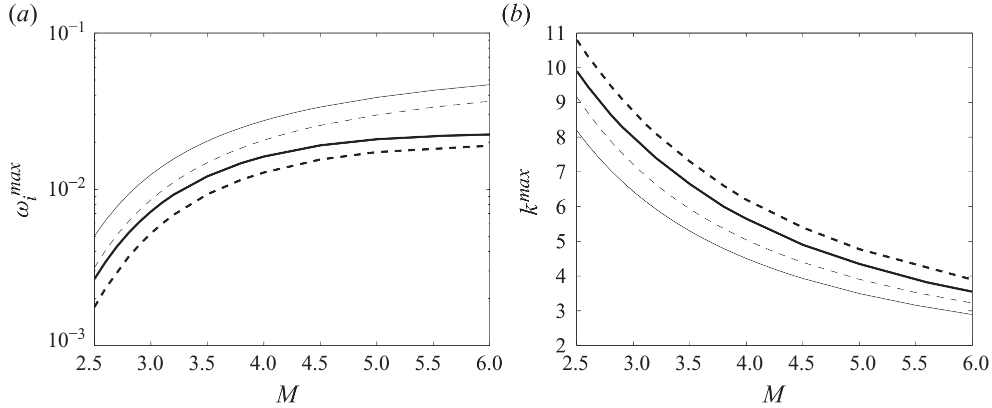

FIGURE 11. Theoretical prediction (thick lines) and numerical value (thin line) of the maximum growth rate (*a*) and of the most dangerous wavenumber (*b*) as a function of the Mach number M for the branch label $n = 4$ for two values of m: $m = 0$, solid line; $m = 1$, dashed line.

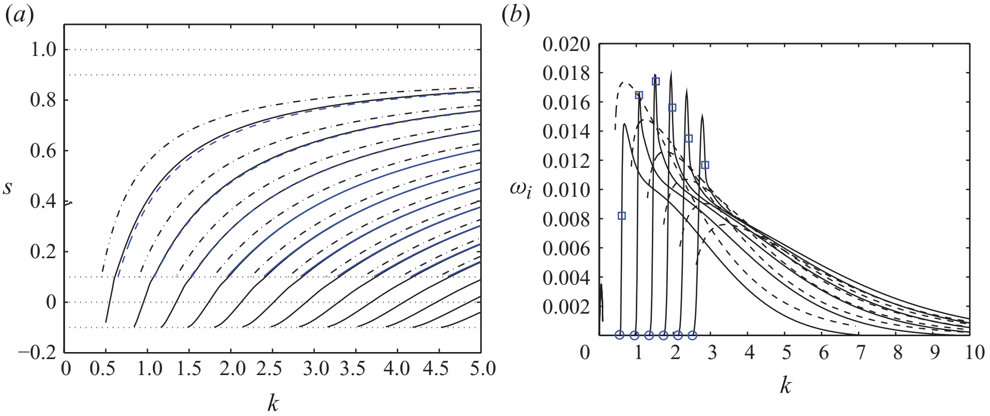

FIGURE 12. (Colour online) Phase velocity (*a*) and growth rate (*b*) with respect to axial wavenumber for $M = 10$ and $m = 1$. The solid line shows collocation results, the dashed line theoretical predictions for high Mach numbers and the dash-dotted theoretical predictions for low Mach number are given. In (*b*), only the first five branches are shown.

estimated by the hypersonic formula. For the case of $k = M$, the hypersonic formula is able to capture almost the exact value of the growth rate for Mach numbers higher than 8.

5. Applications

For the jet considered here, we have seen that for large Mach numbers the most unstable mode tends to become a supersonic coflow mode different from the Kelvin–Helmholtz mode. By its acoustic signature in the far field, this supersonic unstable mode is expected to be an important contribution of the noise induced by the jet instability. We can then naturally think that the noise induced by instability will diminish if the mode itself becomes less unstable. It is this strategy that can be used to control the noise generated by the jet. By using the expressions obtained above

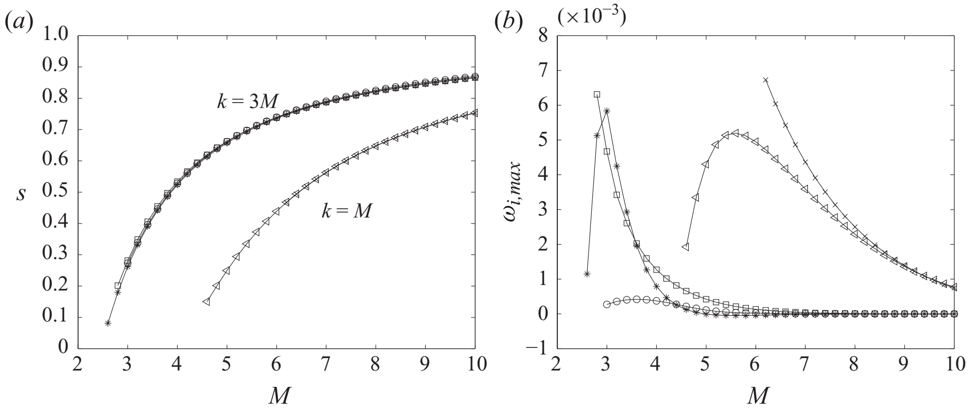

FIGURE 13. Comparison of theoretical and numerical results for the fourth supersonic axisymmetric mode when $k = 3M$ and $k = M$. (*a*) Phase velocity s_r versus M. (*b*) Growth rate ω_i versus M. Numerical results are indicated by (∗) and (×) for $k = 3M$ and $k = M$, respectively. Theoretical results obtained from the hypersonic flow formula (4.31) are plotted with the symbols (○) and (◁) for $k = 3M$ and $k = M$, respectively. Formulas (4.24) and (4.25) are obtained when $k \gg M$ are plotted with the symbol (□).

for the instability growth rate, we are going to show that known effects of base-flow modifications can be easily predicted.

We have seen that the growth rate of supersonic modes depends in an exponential way on integrals between the turning points and the critical point and that if the distance between these points increases the growth rate decreases. This property can be used to modify the base flow in an appropriate way. In figure 14, we plot the turning point and critical point locations when a sonic coflow is added to the base flow slightly outside the main jet. In this figure, we clearly see that the distance between the critical point and the second turning point is increased with coflow, whereas the position of the first critical point is not affected for $s > 0$. By applying formula (4.24), we then deduce that the relation between the wavenumber and the phase velocity of the mode is not modified, and therefore, by applying formula (4.25) that the growth rate is decreased in the presence of coflow. As a consequence, noise should be weaker with coflow. This is indeed what is observed in the experiments (see Papamoschou & Debiasi 2001). More precisely, this simple argument can explain why the larger the diameter of the coflow, the more efficient the noise reduction.

More complicated jet modifications could also be considered as long as the critical and turning point structure of figure 4(*b*) is maintained. In that case, the general growth rate formulas can be used. The impact on noise emission can then easily be inferred from the growth rate variations.

6. Conclusion

A comprehensive stability diagram has been obtained for a model of supersonic jets for Mach numbers ranging from 1 to 10. In addition to the well-known Kelvin–Helmholtz modes, three different families of modes (subsonic counterflow modes, subsonic coflow modes and supersonic coflow modes) have been identified, the last two being unstable. The spatial structure of all these modes, as well as their dispersion relation have been obtained for arbitrary jet profiles by using a WKBJ analysis in the limit of large axial wavenumber. A special expression has also been

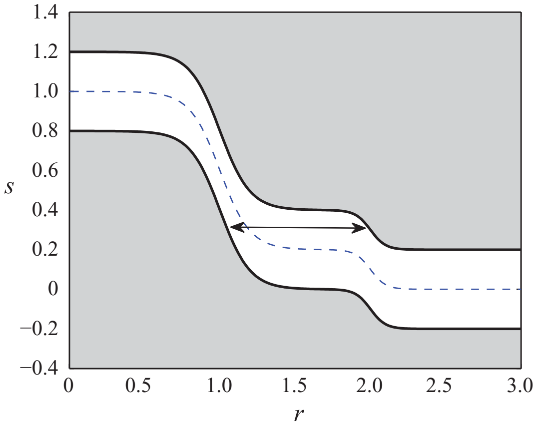

FIGURE 14. (Colour online) Turning point and critical point locations as a function of the phase velocity (y-axis). A sonic coflow is added to a supersonic jet at $M = 5$.

obtained in the hypersonic limit where both k and M are large and of the same order.

The theoretical results have been compared to the numerical results obtained for a jet model and a good agreement has been demonstrated, especially for the spatial structure and the phase velocity of the modes. The variation of the growth rate of the unstable modes has been shown to be in good agreement with the numeric. This has permitted us to propose a means of control of the radiated sound associated with these modes in hypersonic jets. We have shown that a known effect of coflow on the jet noise can be easily predicted by the theory.

L.P. would like to thank Spanish MEC for its financial support by a postdoctoral fellowship EX-2007-0515.

Appendix. Details of the WKBJ analysis

In this appendix, we provide the local solutions near the origin, a turning point and a critical point that have been used to obtain the relation between the WKBJ approximation in the different regions.

We start with the solution near the origin, which has to be obtained to apply the boundary condition at $r = 0$. A similar analysis is performed in Le Dizès & Lacaze (2005).

A.1. *Near axis solution*

The WKBJ solutions are singular at the origin owing to the presence of a regular singularity in (2.9). The local solution is obtained by introducing the local variable $\bar{r} = kr$. Equation (2.9) becomes near the origin with this new variable

$$\frac{\mathrm{d}^2 p_0}{\mathrm{d}\bar{r}^2} + \frac{1}{\bar{r}}\frac{\mathrm{d}p_0}{\mathrm{d}\bar{r}} + \left(\beta_0^2 - \frac{m^2}{\bar{r}^2}\right) p_0 = 0, \tag{A 1}$$

where $\beta_0 = \beta(0) = \sqrt{M^2(1-s)^2 - 1}$ is a real positive number if $s < 1 - 1/M$ (which corresponds to the situation analysed here). The solution which remains bounded at the origin is

$$p_0(\bar{r}) = a_0 J_{|m|}(\beta_0 \bar{r}). \tag{A 2}$$

From the behaviour of the Bessel function $J_{|m|}$ for large $\bar{r}$, we deduce the expression (written with the outer variable r)

$$p_0(r) \sim a_0 \left(\frac{2}{\pi k r \beta_0}\right)^{1/2} \cos\left(\beta_0 k r - \frac{|m|\pi}{2} - \frac{\pi}{4}\right), \tag{A 3}$$

which matches with the WKBJ expression (4.10) as r goes to zero for an appropriate choice of the constant a_0.

A.2. *Near turning point solution*

The turning point is a point where β^2 vanishes. We consider a single turning point r_t, that is a non-degenerate zero of β^2 where β^2 changes sign. We assume here that $\beta^2 > 0$ for $r < r_t$ and $\beta^2 < 0$ for $r > r_t$. The local analysis near a turning point is very classical (see for instance Bender & Orszag 1999) and requires the introduction of the local variable $\tilde{r} = k^{2/3}(r - r_t)$. Equation (2.9) becomes near r_t with this variable an Airy equation

$$\frac{\mathrm{d}^2 p_t}{\mathrm{d}\tilde{r}^2} - \alpha \tilde{r} p_t = 0, \tag{A 4}$$

where $\alpha = -\partial_r(\beta^2)(r_t)$ is a positive real number. The general solution of this equation is

$$p_t(\tilde{r}) = A_t \mathrm{Ai}(\alpha^{1/3}\tilde{r}) + B_t \mathrm{Bi}(\alpha^{1/3}\tilde{r}), \tag{A 5}$$

where Ai and Bi correspond to Airy functions of the first and second kind.

From the behaviour of Airy functions for large arguments, we can deduce the following expression far from the turning point as $\tilde{r} \to \infty$:

$$p_t \sim \pi^{-1/2} \left(\alpha^{1/3} k^{2/3} |r - r_t|\right)^{-1/4} \left(\tfrac{1}{2} A_t \,\mathrm{e}^{-\frac{2}{3}\alpha^{1/2} k |r - r_t|^{3/2}} + B_t \,\mathrm{e}^{\frac{2}{3}\alpha^{1/2} k |r - r_t|^{3/2}}\right), \tag{A 6}$$

and as $\tilde{r} \to -\infty$

$$\begin{aligned} p_t \sim \pi^{-1/2} \left(\alpha^{1/3} k^{2/3} |r - r_t|\right)^{-1/4} \Big(A_t \sin\left(\tfrac{2}{3}\alpha_t^{1/2} k |r - r_t|^{3/2} + \pi/4\right) \\ + B_t \cos\left(\tfrac{2}{3}\alpha^{1/2} k |r - r_t|^{3/2} + \pi/4\right)\Big). \end{aligned} \tag{A 7}$$

From these expressions, it is straightforward to obtain the relations (4.6*a*, *b*) that connect the WKBJ approximations on each side of the turning point.

A.3. *Near critical point solution*

A critical point is a point where $s = W$. The analysis of the solution near a critical point in the limit of large wavenumber has already been performed by Le Dizès & Billant (2009). As discussed by Le Dizès & Billant (2009), we shall see that the critical point is responsible for a singularity at the second order.

Near a critical point, the local variable is $\check{r} = k(r - r_c)$. With this new variable, (2.9) becomes as $k \to \infty$ up to $O(1/k^2)$ terms:

$$\frac{\mathrm{d}^2 p_c}{\mathrm{d}\check{r}^2} + \left(-\frac{2}{\check{r}} + \frac{L}{k}\right)\frac{\mathrm{d}p_c}{\mathrm{d}\check{r}} - p_c = 0, \tag{A 8}$$

with

$$L = \frac{1}{r_c} - \frac{\rho_c'}{\rho_c} - \frac{W_c''}{2W_c'}. \tag{A 9}$$

The general solution of this equation can be written as

$$p_c(\breve{r}) = A_c\left((1-\breve{r})\,\mathrm{e}^{\breve{r}} + \frac{L}{k}(1+\breve{r})\ \mathrm{e}^{-\breve{r}}\left(\left(\frac{\breve{r}+\log\breve{r}}{2} - \frac{3}{4} - \frac{\log\breve{r}}{1+\breve{r}}\right)\mathrm{e}^{2\breve{r}} - \frac{1}{2}\int_{-\infty}^{\breve{r}}\frac{\mathrm{e}^{2u}\,\mathrm{d}u}{u}\right)\right)$$
$$+ B_c\left((1+\breve{r})\,\mathrm{e}^{-\breve{r}} + \frac{L}{k}(1-\breve{r})\,\mathrm{e}^{\breve{r}}\left(\left(\frac{\breve{r}-\log\breve{r}}{2} + \frac{3}{4} + \frac{\log\breve{r}}{1-\breve{r}}\right)\mathrm{e}^{-2\breve{r}} - \frac{1}{2}\int_{\infty}^{\breve{r}}\frac{\mathrm{e}^{-2u}\,\mathrm{d}u}{u}\right)\right). \tag{A 10}$$

It is valid up to $O(1/k^2)$ terms and assumes implicitly that $M=O(1)$. If we keep the main contribution of both the dominant and subdominant terms we obtain (written with outer variable), as $\breve{r}$ goes to $+\infty$,

$$p_c \sim k|r-r_c|\left[-A_c\,\mathrm{e}^{k|r-r_c|} + \left(B_c + \mathrm{i}\frac{\pi L}{2k}A_c\right)\ \mathrm{e}^{-k|r-r_c|}\right], \tag{A 11}$$

and as $\breve{r}$ goes to $-\infty$,

$$p_c \sim k|r-r_c|\left[\left(A_c - \mathrm{i}\frac{\pi L}{2k}B_c\right)\ \mathrm{e}^{-k|r-r_c|} - B_c\,\mathrm{e}^{k|r-r_c|}\right]. \tag{A 12}$$

From these expressions, we can easily obtain the connection formulas

$$\mathrm{e}^{-v(r_c,r)} \longleftrightarrow -\ \mathrm{e}^{v(r_c,r)} + \frac{L\pi\mathrm{i}}{2k}\,\mathrm{e}^{-v(r_c,r)}, \tag{A 13a}$$

$$-\,\mathrm{e}^{v(r_c,r)} - \frac{L\pi\mathrm{i}}{2k}\,\mathrm{e}^{-v(r_c,r)} \longleftrightarrow \mathrm{e}^{-v(r_c,r)}, \tag{A 13b}$$

from which we can deduce the other connection formula

$$\mathrm{e}^{v(r_c,r)} \longleftrightarrow \frac{\mathrm{i}L\pi}{2k}\,\mathrm{e}^{+v(r_c,r)} - \left(1 - \frac{\pi^2L^2}{4k^2}\right)\,\mathrm{e}^{-v(r_c,r)}. \tag{A 14}$$

Note the non-reversibility of the connection formulas (A 13*a*, *b*). This is associated with the critical point singularity which has to be avoided in the upper half plane in (A 10). This condition breaks the ($\breve{r} \to -\breve{r}$) symmetry.

A.4. *Near critical point solution in the high Mach number case*

When M becomes of order $O(k)$, the two turning points and the critical point are merged at leading order as k goes to infinity. The solution near such a point is particular and is considered in this section in order to obtain the connection formulas between both WKBJ approximations valid on either side of that point.

We first define the rescaled Mach number $M_0 = M/k$ and introduce the local variable $\breve{r} = k(r-r_c)$. With this variable, (2.9) becomes near r_c

$$\frac{\mathrm{d}^2p_c}{\mathrm{d}\breve{r}} - \frac{2}{\breve{r}}\frac{\mathrm{d}p_c}{\mathrm{d}\breve{r}} + \left(\lambda_c^2\breve{r}^2 - 1\right)p_c = 0, \tag{A 15}$$

where $\lambda_c = M_0|W_c'|/c$ is a real positive number. The general solution of this equation can be expressed in terms of the confluent hypergeometric function $U(a,b,z)$ (see Abramowitz & Stegun 1965):

$$p_c(\breve{r}) = \breve{r}^3\left(C_1\,\mathrm{e}^{\mathrm{i}\pi(a-b)}\,\mathrm{e}^{z/2}z^{b/2}U(b-a,b,-z) + C_2\,\mathrm{e}^{-z/2}z^{b/2}U(a,b,z)\right), \tag{A 16}$$

with $a = 5/4 - \mathrm{i}/(4\lambda_c)$, $b = 5/2$ and $z = \mathrm{i}\lambda_c\breve{r}^2$.

From the behaviour of $U(a,b,z)$ as $|z|\to\infty$ with $\arg(z)=\pm\pi/2$ ($\breve{r}\to\infty$) and $\arg(z)=3\pi/2$, $5\pi/2$ ($\breve{r}\to-\infty$), we can deduce the following expressions of p_c (written with the outer variable) as $\breve{r}\to\infty$:

$$p_c \sim k^{1/2}|r-r_c|^{1/2}\left[C_1\,\mathrm{e}^{z/2}|r-r_c|^{-\mathrm{i}/(2\lambda_c)}\kappa^{-\mathrm{i}} + C_2\,\mathrm{e}^{-z/2}|r-r_c|^{\mathrm{i}/(2\lambda_c)}\kappa^{\mathrm{i}}\right], \tag{A 17}$$

and as $\breve{r}\to-\infty$

$$\begin{aligned} p_c \sim k^{1/2}|r-r_c|^{1/2}\Bigg[&\left(\mathrm{e}^{2\mathrm{i}\pi a}C_1 - 2\cos(\pi a)\frac{\Gamma(b-a)}{\Gamma(a)}C_2\right)\mathrm{e}^{z/2}|r-r_c|^{-\mathrm{i}/(2\lambda_c)}\kappa^{-\mathrm{i}} \\ &+\left(-\,\mathrm{e}^{2\mathrm{i}\pi a}C_2 + 2\mathrm{i}\sin(\pi a)\,\mathrm{e}^{2\mathrm{i}\pi a}\frac{\Gamma(a)}{\Gamma(b-a)}C_1\right)\mathrm{e}^{-z/2}|r-r_c|^{\mathrm{i}/(2\lambda_c)}\kappa^{\mathrm{i}}\Bigg], \end{aligned} \tag{A 18}$$

where in both formulas z is now $z=\mathrm{i}\lambda_c k|r-r_c|^2$, and $\kappa=(\mathrm{i}\lambda_c k^2)^{1/(4\lambda_c)}$. We then obtain the following connection formulas for the WKBJ approximation on each side of the critical point:

$$\mathrm{e}^{2\mathrm{i}\pi a}\,\mathrm{e}^{\mathrm{i}\tilde{u}(r_c,r)} + \frac{2\mathrm{i}\sin(\pi a)}{\kappa^{2\mathrm{i}}}\,\mathrm{e}^{2\mathrm{i}\pi a}\frac{\Gamma(a)}{\Gamma(b-a)}\,\mathrm{e}^{-\mathrm{i}\tilde{u}(r_c,r)} \longleftrightarrow \mathrm{e}^{\mathrm{i}\tilde{u}(r_c,r)}, \tag{A 19a}$$

$$-2\cos(\pi a)\frac{\Gamma(b-a)}{\Gamma(a)}\kappa^{2\mathrm{i}}\,\mathrm{e}^{\mathrm{i}\tilde{u}(r_c,r)} - \mathrm{e}^{2\mathrm{i}\pi a}\,\mathrm{e}^{-\mathrm{i}\tilde{u}(r_c,r)} \longleftrightarrow \mathrm{e}^{-\mathrm{i}\tilde{u}(r_c,r)}. \tag{A 19b}$$

REFERENCES

Abramowitz, M. & Stegun, I. A. 1965 *Handbook of Mathematical Functions*. Dover.

Batchelor, G. K. & Gill, A. E. 1962 Analysis of the stability of axisymmetric jets. *J. Fluid Mech.* **14**, 529–551.

Bender, C. M. & Orszag, S. A. 1999 *Advanced Mathematical Methods for Scientists and Engineers*. Springer.

Blumen, W. 1970 Shear layer instability of an inviscid compressible fluid. *J. Fluid Mech.* **40**, 769–781.

Blumen, W., Drazin, P. G. & Billings, D. F. 1975 Shear layer instability of an inviscid compressible fluid. Part 2. *J. Fluid Mech.* **71**, 305–316.

Drazin, P. G. & Howard, L. N. 1966 Hydrodynamic stability of parallel flow of inviscid fluid. *Adv. Appl. Mech.* **9**, 1–89.

Duck, P. 1990 The inviscid axisymmetric stability of the supersonic flow along a circular cylinder. *J. Fluid Mech.* **214**, 661–637.

Fabre, D. & Jacquin, L. 2004 Viscous instabilities in trailing vortices at large swirl numbers. *J. Fluid Mech.* **500**, 239–262.

Landau, L. 1944 Stability of tangential discontinuities in compressible fluid. *Akad. Nauk. S.S.S.R., Comptes Rendus (Doklady)* **44**, 139–141.

Lau, J. C. 1981 Effects of exit mach number an temperature on mean flow and turbulence characteristics in round jets. *J. Fluid Mech.* **105**, 193–218.

Le Dizès, S. 2008 Inviscid waves on a Lamb–Oseen vortex in a rotating stratified fluid: consequences on the elliptic instability. *J. Fluid Mech.* **597**, 283–303.

Le Dizès, S. & Billant, P. 2009 Radiative instability in stratified vortices. *Phys. Fluids* **21**, 096602.

Le Dizès, S. & Lacaze, L. 2005 An asymptotic description of vortex kelvin modes. *J. Fluid Mech.* **542**, 69–96.

Lighthill, M. J. 1952 On sound generated aerodynamically. I. General theory. *Proc. R. Soc. Lond.* A **211**, 564–587.

Lindzen, R. & Barker, J. W. 1985 Instability and wave over-reflection in stably stratified shear flow. *J. Fluid Mech.* **151**, 189–217.

Luo, K. H. & Sandham, N. D. 1996 Instability of vortical and acoustic modes in supersonic round jets. *Phys. Fluids* **9**, 1003–1013.

Mack, L. M. 1984 Boundary layer linear stability theory. *AGARD Rep.* 709.

Mack, L. M. 1990 On the inviscid acoustic-mode instability of supersonic shear flows. Part I. Two-dimensional waves. *Theor. Comput. Fluid Dyn.* **2**, 97.

Michalke, A. 1964 On the inviscid instability of the hyperbolic-tangent profile. *J Fluid Mech.* **19**, 543–556.

Papamoschou, D. & Debiasi, M. 2001 Directional suppression of noise from a high-speed jet. *AIAA* **39** (3), 380–387.

Riedinger, X., Le Dizès, S. & Meunier, P. 2010 Viscous stability properties of Lamb–Oseen vortex in a stratified fluid. *J. Fluid Mech.* **645**, 255–278.

Shepard, H. K. 1983 Decay widths for metastable states. Improved WKB approximation. *Phys. Rev.* D **27** (6), 1288–1298.

Takehiro, S. & Hayashi, Y. Y. 1992 Over-reflection and shear instability in a shallow-water model. *J. Fluid Mech.* **236**, 259–279.

Tam, C. W. 1995 Supersonic jet noise. *Annu. Rev. Fluid Mech.* **27**, 17–43.

Tam, C. K. W. & Burton, D. E. 1984*a* Sound generated by instability waves of supersonic flows. Part 1. Two-dimensional mixing layers. *J. Fluid Mech.* **138**, 249–271.

Tam, C. K. W. & Burton, D. E. 1984*b* Sound generated by instability waves of supersonic flows. Part 2. Axisymmetric jets. *J. Fluid Mech.* **138**, 273–295.

Tam, C. K. W. & Hu, F. Q. 1989 On the three families of instability waves of high speed jets. *J. Fluid Mech.* **201**, 447–483.

Troutt, T. R. & McLaughlin, D. K. 1982 Experiments of the flow and acoustic properties of a moderate-Reynolds-number supersonic jet. *J. Fluid Mech.* **116**, 123–156.